
Article:
Toperesu, PM, Kale, GM orcid.org/0000-0002-3021-5905, Daji, J et al. (1 more author) (2021) Development and evolution of a novel (Zr1-xSnx)O2 toughened alumina-mullite slip cast refractory: Effect of SnO2. Journal of the European Ceramic Society, 41 (3). pp. 2134-2144. ISSN 0955-2219

https://doi.org/10.1016/j.jeurceramsoc.2020.10.070

Development and Evolution of a Novel $(Zr_{1-x}Sn_x)O_2$ toughened Alumina-Mullite Slip Cast Refractory: Effect of SnO_2.

Phillip Masimba Toperesu,[a,b] Girish M. Kale,[a],* Jafar Daji[b] and David Parkinson[b]

[a]School of Chemical and Process Engineering, University of Leeds, Leeds LS2 9JT, U.K.
[b]Parkinson-Spencer Refractories Ltd, Halifax HX3 6SX, U.K.

*Author for all correspondences: g.m.kale@leeds.ac.uk (E); 0044-113-3432805 (T)

Abstract

$Zr_{1-x}Sn_xO_2$ reinforced alumina-mullite refractory was manufactured by slip cast methods using SnO_2 as a sintering agent. SnO_2 had considerable influence in the enhanced reaction kinetics of zircon dissociation and subsequent reaction sintering of alumina and zircon. Presence of pro-eutectic transient Al_2O_3-SnO_2 liquid and SnO_2-SiO_2-ZrO_2 amorphous phases, enhanced densification and mullitisation through liquid phase sintering and, mitigated SnO_2 volatilisation by $(Zr_{1-x}Sn_x)O_2$ solid-solution formation. Based on their morphology and aspect ratios, three types of mullite crystals, MI, MII and MIII, were evolved across the matrix microstructure. Characterization of the evolved microstructure revealed coalescence and grain growth of matrix alumina grains including the presence of an acicular tertiary MIII mullite which acts as both a reinforcement and bridging network of matrix to aggregate grains. SnO_2 had the effect of lowering the monoclinic – tetragonal phase transformation temperature. Hot flexural strength values remained nearly unchanged (±2%) compared with the AZS composition without SnO_2 doping.

Keywords: Tin IV oxide; reinforced acicular mullite; alumina, $Zr_{1-x}Sn_xO_2$ solid solution, Refractories.

Funding Sources: This research did not receive any specific grant from funding agencies in the public, commercial, or not-for-profit sectors.

1 Introduction

Zirconia reinforced mullite refractories from the Al_2O_3-ZrO_2-SiO_2 (AZS) and Al_2O_3-ZrO_2-$Al_6Si_2O_{13}$ (AZM) systems have a wide range of application in the glass industries, both as structural applications (e.g.,super-structure, crown) and glass contact applications (channels blocks and forehearth) [1-4]. This is due to their excellent thermo-mechanical properties such as low thermal expansion and low creep rate at high-temperatures (inherent from the mullite phase); and, the excellent fracture toughness as well as chemical stability in alkaline siliceous melts (coming from the zirconia phases) [2-5]. Zirconia has been shown from wettability and corrosion studies, not to be easily wetted or soluble in siliceous melts and hence the addition of ZrO_2 to the mullite based refractory composites is widely practiced to enhance their chemical stability in glass melts or slags [4,6].

Mullite composition can be expressed as $Al_{4+2x}Si_{2-2x}O_{10-2x;}$ x = 0.2 – 0.5 where x denotes the non-stoichiometric range of the number of oxygen vacancies formed per average unit cell. This is the only stable crystalline non-stoichiometric solid solution composition in the Al_2O_3 – SiO_2 binary system under standard conditions [7]. Mullite compositions with x = 0.25 (71 – 76 wt. % Al_2O_3); and x = 0.4 (>76 wt. % Al_2O_3) have been described as 3:2 mullite ($3Al_2O_3{\cdot}2SiO_2$) and 2:1 mullite ($2Al_2O_3{\cdot}SiO_2$) respectively [7]. The coefficient of thermal expansion of 2:1 mullite composition is lower and less anisotropic than that of the 3:2 compositions [8]. At room temperature, mullite suffers from low fracture toughness and relatively low strength, compared to the other ceramic compounds [7,8]. Improvements or increase in the K_{IC} and strength have been shown to be realised through incorporation of ZrO_2 into the ceramic composites, thereby reinforcing the matrix [5-8]. Synthesis of zirconia toughened mullite composites is widely achieved by various processing routes [5,8,9]; and reaction sintering of Al_2O_3 and zirconium silicate ($ZrSiO_4$) bearing compounds being one of the proven cheaper and extensively explored method of producing zirconia reinforced mullite composites [8-10].

Zircon ($ZrSiO_4$) as a raw material is available in abundance and a cheap source of zirconia [8-10].

The microstructural evolution of the crystallised fraction, composition and morphology of mullite from the conventional reaction sintering of micro to macro-sized zircon and alumina mix formulations is reported to be dependent on the firing conditions [7-11]. The microstructure of Mullite, either fused cast or formed in the presence of a liquid phase always exhibits an acicular morphology [11-13]. However that formed by solid state sintering and in the absence of a liquid phase is normally granular and varies depending on the nature and purity of the starting raw materials [8,11,13]. In the absence of impurities, only some detectable amounts of mullite are formed when sintering above 1400 °C, with complete mullite conversion requiring sintering at temperatures in the proximity of 1700 °C [7,8, 9].

Work by Iqbal and Lee [11,13] led to their proposed nomenclature (based upon the morphology and relative aspect ratios) of the different types of mullite that they observed to have evolved from porcelain fired products. They named the cuboidal, granular low aspect ratio (1-3:1) grains as primary mullite "Type 1 (MI);" Secondary mullite, "Type 2 (MII)" for high aspect ratio (3-10:1) and "Type 3 (MIII)" for very high aspect ratio (30-40:1) acicular mullite [11-13]. Another form of acicular mullite, formed in the presence of an alumina rich liquid phase and/or from the edges of alumina grains into the glassy phase, was observed and named "Type 3 (MIII)" tertiary mullite [13]. Reaction sintering of stoichiometric 3:2 mullite occurs according to the following reaction;

$$3Al_2O_{3(s)} + 2ZrSiO_{4(s)} + (CaO/TiO_2/MgO)/heat = Al_6Si_2O_{13} + 2ZrO_2 \quad \ldots\ldots\ldots\ldots\ldots\ldots \quad (1)$$

where, CaO [14]; TiO_2 [15-18]; MgO [19,20]; La_2O_3 [21]; Dy_2O_3 [22]; are some of the additives employed in the starting formulation mix, as sintering agents, that have been reported in the literature to enhance densification and/or mullitisation through liquid phase sintering

from the dissociated zircon and lowering of the mullitisation temperature [14-22]. Among these reported additives, TiO_2 additions up to 4wt. % has been extensively studied and reported to enhance mullitisation considerably through the formation of $ZrTiO_3$ and solubility in the evolved mullite [15-18]. However, addition of TiO_2 has been reported to deteriorate hot flexural strength [15,16] of refractory bodies by about 25%. Addition of B_2O_3 into a biphasic gel was also reported to lower mullitisation temperature through reduction in viscosity of the SiO_2-rich amorphous phase [23]. The mullitisation effect of pentavalent oxides V_2O_5, Nb_2O_5 and Ta_2O_5 on (SiO_2 and Al_2O_3) mullite precursors was investigated by Kong et al [24], reporting that only V_2O_5 enhanced mullitisation while Nb_2O_5 and Ta_2O_5 inhibited mullite formation.

The use of SnO_2 in reaction sintering of mullite has not been extensively reported although several publications have reported on the formation of a $(Zr_{1-x}Sn_x)O_2$ solid solution in the zirconia rich-end of the ZrO_2-SnO_2 binary system [25-29]. Maximum SnO_2 solid solubility in ZrO_2 was found to be ca. 20 mol. %; while some studies [28,29] found out that partial stabilization of the metastable ZrO_2 and suppression of its transition to the monoclinic polymorph can be achieved at lower temperatures but not as effective to room temperature. Kong et al, investigated the mullitisation effects of oxides such as SnO_2, Sb_2O_3 and Bi_2O_3 on quartz and Al_2O_3, oxide mixtures [30]. They reported increased mullitisation from Sb_2O_3 and Bi_2O_3 additions, but negligible effect on mullite formation in the presence of SnO_2 up to 1500 °C [30]. Yin et al [31] conducted a critical evaluation and optimization of the SnO-SnO_2-SiO_2 system by heating and quenching techniques of SnO_2 and SiO_2 mixed powders in a Rhenium crucible covered in a platinum outer crucible. In their studies, Yin et al [31] found no solid solubility in the SnO_2 – SiO_2 system however they observed a eutectic of SnO_2 and SiO_2 in the SiO_2 rich regions at eutectic temperatures of 1500 °C - 1510 °C and a liquid miscibility gap in

the SnO_2 rich regions at monotectic temperatures of 1625 °C – 1650 °C. In the Al_2O_3-SnO_2 system, the eutectic temperature is found to be at 1620 °C ± 5 °C [32].

SnO_2 has the same rutile structure as TiO_2, and as such we expected it to have comparable properties and effect on the reaction sintering of zircon and alumina raw materials akin to rutile (TiO_2). In addition, it is also known that amongst non-colouring oxides, SnO_2 presents the lowest solubility in soda-lime and borosilicate glasses with the order of solubility reported as; SiO_2 > Al_2O_3 > ZrO_2 > SnO_2 > Cr_2O_3 [33]. Therefore, incorporation of SnO_2 into the AZS/AZM microstructure and matrix would be expected to enhance the chemical compatibility of the refractory composites in glass melts. However, SnO_2 has a melting point of 1625 °C ± 5 °C; and is known to volatise at these temperatures. Therefore, in the present study, the effect of SnO_2 as a sintering aid on the reaction sintering of $ZrSiO_4$ and Al_2O_3 mixtures to produce zirconia toughened mullite composites was studied from 1500 °C – 1570 °C to avoid potential loss of SnO_2 due to volatisation.

2 Materials and Methods

2.1 Materials

Three, medium to coarse commercial grade, size-fractions of tabular alumina (d_{50} = 850µm; 1040µm and 1250µm); reactive alumina; prime calcined zircon sand (d_{50} = 140µm) and zircon flour (d_{50} = 2.5µm) were used as the main raw material components. Pure Reagent grade (>99.9%) SnO_2 (Keeling Walker Ltd, Stoke-on-Trent) was used as the sintering aid.

For this study, an AZS refractory composition, designated AZS-01 was made from 5kg batches of alumina and zircon starting mix formulations. To evaluate the effects of SnO_2 as a sintering aid, the AZS-01 batch was incorporated with 5 wt. % SnO_2 to form another composition, designated AZS-T1 by removing 5 wt. % of alumina fractions while keeping the zircon content constant. About 1 wt.% of Kaolin clay – d_{50} = 2.5µm; with chemical analysis of (56.8 wt.%

SiO_2; 39.2 wt.% Al_2O_3; 3.00 wt.% K_2O; 0.43 wt.% Fe_2O_3; 0.48 wt.% TiO_2), was used as both a binder and source of mullite seed nuclei. Clays, such as Kaolin and Ball clays are widely used inorganic binders as they offer high plasticity to the non-plastic refractory raw materials and hence, binding green strength during the forming processes [2,3;11]. Darvan 7, a sodium polymethacrylate dispersant was used as the deflocculant and water as the dispersing medium in slip preparation.

2.2 Methods

In our preliminary research, consolidation of AZS refractory compositions with an initial starting zircon content of > 35wt%; (without the use of any mineralisers); exhibited a loss of densification of the refractories [34]. This was highlighted by the deterioration of the physical properties as observed with an increase in the apparent porosity and subsequent decrease in their bulk densities. Therefore, for this study, with the use of SnO_2 as a sintering aid and mineraliser, refractory compositions with higher ZrO_2 contents were formulated, representing an initial starting zircon content of more than 35 wt.%.

2.2.1 Development of Refractory Composition

The AZS-01 refractory composition, designed from 5kg batches, contained alumina**:**zircon starting mix-formulations in wt. % ratio of 62**:**38. Therefore, to evaluate the effects of SnO_2 as a sintering aid; the AZS-T1, a tin-oxide incorporated derivative of AZS-01, was produced from an alumina-zircon-cassiterite starting mix-formulation in wt. % ratio of 57**:**38**:**5.

The corresponding composite mix formulations of AZS-01 and AZS-T1 were then optimised using the Dinger and Funk model for particle packing to attain optimally packed self-flowing mix fractions. The Dinger and Funk model for particle packing is used extensively for designing the refractory castables [35] and is described by the continuous particle size distribution equation;

$$CPFT/100 = (d^q - d_m^q)/\ D^q - d_m^q) \quad \text{..... (2)}$$

Where; *CPFT* is the (Cumulative Volume Percent Finer Than); *d* is the particle size; *D* is the maximum particle size; d_m is minimum particle size in the distribution; and *q* is the distribution modulus/coefficient (q-value). The Elkem Material Mix Analyzer software (EMMA 3.5.1) was used to determine the optimal packing ratios of each formulation.

Preliminary experiments from our previous studies had shown that a mix formulation with a *q* value of 0.23 provided an optimised mix formulation that exhibited self-flow characteristics with low water demand and optimal packing properties [34]. In the same studies, the use of both zircon sand (d_{50} = 140µm) and zircon flour (d_{50} = 2.5µm and d_{90} = 13.44µm) in the mix formulation was observed to provide a composite alumina-zircon mix formulation with optimum packing, low water demand and self -flow properties when modeled using the Dinger and Funk curve for particle packing at q-value of 0.23.

2.2.2 Slip Preparation, Casting & Sintering

Both the AZS-01 and the tin-oxide incorporated AZS-T1 refractories were produced by slip-casting methods. For slip preparation, the respective optimised mix formulations of AZS-01 and AZS-T1 were dry mixed in a Hobart mixer for 3 minutes. A sodium polymethacrylate dispersant, and water were added and the mixture was mixed for 5 minutes until a homogenous slip was formed.

The prepared slips of AZS-01 and AZS-T1 refractory compositions were slip cast into 50mm depth × 50mm diameter cylindrical gypsum moulds for bulk density and porosity test samples; and into 300mm × 200mm prism gypsum block moulds for refractory under load (RUL) test samples. The test samples were left overnight in the moulds to develop green strength, and then dried in an electric oven at 120 °C for 5 hrs.

To evaluate the effect of SnO_2 as a sintering aid on refractory compositions of the AZS system; batches of the dried green cast samples from the AZS-01 and AZS-T1 refractory compositions were each sintered for 1hr; at similar heating and cooling rates of 3° C/min in a Nalbetherm electric furnace at sintering temperatures of 1500 °C; 1550 °C and 1570 °C respectively.

2.2.3 Physical Property & Thermo-Mechanical tests

The bulk density (BD) and apparent porosity (AP) of the sintered refractory samples were determined using the Archimedes water-immersion technique [36]. The Refractoriness under load (RUL - Differential method with rising temperature) and the Pyrometric Cone Equivalent (PCE) of the sintered refractory compositions were determined according to the BS EN ISO 1893:2008 and ASTM C24-09(2018) standards respectively [37,38].

2.2.4 Chemical (Glass) Compatibility tests.

100mm x 100mm static glass corrosion cup samples of AZS-01 and AZS-T1 refractories with a 25mm diameter x 25mm depth recess cavity in the middle were cast and sintered for Isothermal static glass corrosion tests, according to the ASTM C621 – 09 method.

2.3 Characterisation

Chemical and mineralogical analysis of the sintered refractory products was conducted by XRF and the XRD Bruker D8 X-ray diffractometer (Oxford UNITS). For mineralogical evolution and analysis, a Carl Zeiss EVO MA15 variable pressure W. (tungsten tip) SEM (Oxford Instruments) together with Oxford Instruments Aztec Energy EDX system with 80mm X-Max SDD detector- secondary and backscattered imaging, EDX elemental mapping and line scans plus CZ STEM detector was used on sectioned and polished samples taken off the refractory blocks. A Hitachi SU8230: high performance cold field emission (CFE) SEM with Oxford Instruments, Ultra high resolution, low kV, simultaneous secondary (SE), and backscattered

BSE) imaging; bright field (BF) and dark field (DF) imaging, with nanoscale resolution was used to evaluate the microstructural evolution of the mullite grains in the matrix region.

3 Results and Discussion

3.1 Slip Flow Properties

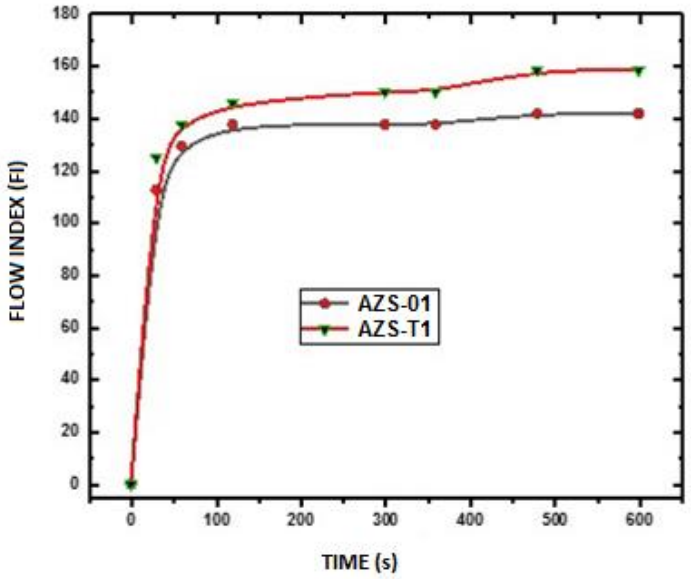

Figure 1: Flow decay characteristic curves of AZS-01 and AZS-T1 refractory slips.

Figure 1 shows the flow decay/flowability characteristic curves of composition AZS-01 and AZS-T1 slips measured over a period of 10 minutes. For shaped or brick casts, this represents an adequate enough period required for the installation or casting and sufficient filling of the slip into the mould before it starts setting [2,7]. The flow characteristics of AZS-01 and AZS-T1 refractory slips, with a solid loading of 94.5% and reduced water demand (< 5.5%), exhibited excellent free flow properties, having a FI ≥ 80%; which is comparable to the standard commercial low cement castables (LCC) and no-cement (NCC) castables with water demand of (> 8%) [2,7]. Lower water demand is deemed to be a more sustainable approach and is also advantageous for improved mechanical and physical properties of sintered products [2,7].

3.2 Effect on the Refractory Microstructural Evolution

The chemical composition of the sintered AZS-01 and AZS-T1 refractories is shown in Table 1.

Table 1: Chemical composition in wt. % of AZS-01 and AZS-T1 refractories sintered at 1550 °C

Sample	Chemical Composition (wt. %)								
	Al_2O_3	SiO_2	ZrO_2	SnO_2	*R_2O	**RO	Fe_2O_3	TiO_2	Others
AZS-01	61.80	12.80	24.90	-	0.21	0.08	0.06	0.09	<0.12
AZS-T1	57.79	12.96	24.55	4.02	0.2	0.08	0.06	0.1	<0.32

* $R_2O = Na_2O + K_2O$; ** RO = CaO

Figure 2 shows the XRD patterns, and phase evolution of refractory samples of composition AZS-01 sintered at 1500 °C and 1550 ˚C for 1 hr; and figure 3 shows the diffraction patterns and phase evolution of AZS-T1 samples sintered at 1500 ˚C and 1550 °C for 1hr respectively. When considering the oxide phase constituents and their relative peak intensities from the diffraction patterns of AZS-01 and AZS-T1 refractories sintered at 1500 °C; corundum and primary zircon are the major phases. For AZS-01, new peaks of mullite and monoclinic ZrO_2 appear as intermediate to minor phases; while in the AZS-T1, the intermediate and minor phases are mullite and $(Zr_{1-x}Sn_x)O_2$ solid solution. The $(Zr_{1-x}Sn_x)O_2$ phase is in monoclinic form and no high-temperature tetragonal phase is retained which is in agreement with observations reported in the literature by other workers [23,24,39]. The presence of zircon peaks suggests of a partial dissociation of either the zircon sand or zircon flour from the starting material. Thus, it is apparent that complete mullitisation was not achieved at 1500 °C even in the presence of SnO_2.

For the AZS-01 refractory samples sintered above 1500 °C; the diffraction pattern of AZS-01 sintered at 1550 ˚C; shown in figure 2, shows an increased intensity of the mullite peaks and a decrease in the zircon peak intensities. An XRD diffraction pattern of the AZS-01 sintered at

1570 °C also showed a similar XRD pattern and no significant changes. The zircon peaks show that the primary $ZrSiO_4$ in AZS-01 remains as the major phase even when sintering at 1550 °C or 1570 °C. This means that with the increased thermal energy, enhanced evolution of mullite from a minor phase to an intermediate/major phase at 1550 °C and or 1570 ˚C does take place in the absence of SnO_2, albeit without the complete dissociation of $ZrSiO_4$.

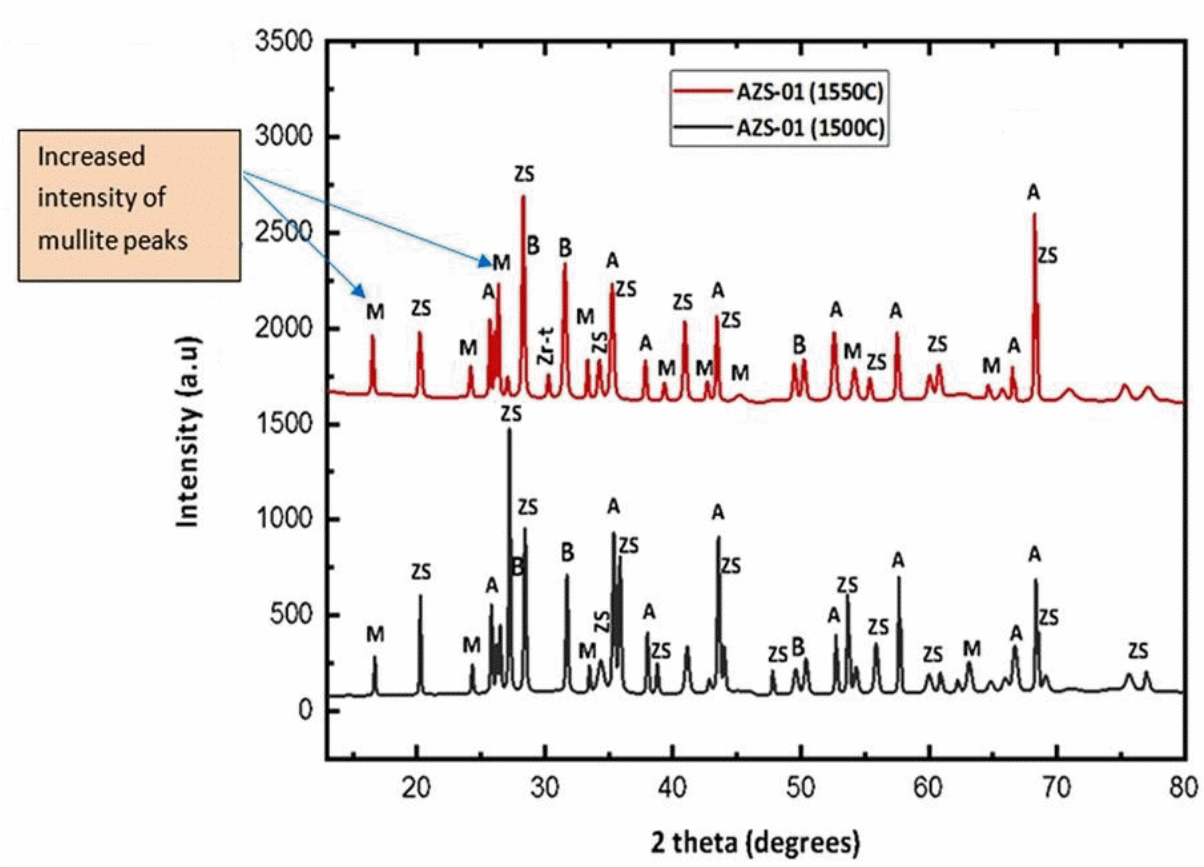

Figure 2: XRD pattern of AZS-01 refractory sintered at 1500 °C and 1550 °C for 1hr. (M =Mullite, ZS = Zircon, A= α-Al_2O_3, B (Baddeleyite) =monoclinic ZrO_2, Zr-t = Tetragonal ZrO_2)

However, in contrast, as shown in figure 3, no zircon peaks are present in the diffraction pattern of the AZS-T1 refractory sintered at 1550 °C; indicating complete dissociation of the zircon grains occurs above 1500 °C in the presence of SnO_2. Figure 3 shows that at 1550 °C, corundum, mullite and $Zr_{1-x}Sn_xO_2$ are the major and only mineralogical phases present. Figure 3 further shows that for the AZS-T1 refractory sintered above 1500 °C, partially stabilised

zirconia as tetragonal $Zr_{1-x}Sn_xO_2$; appears as a new minor phase. This shows that SnO_2 has a significant effect in the dissociation mechanism of zircon and mullitisation of the alumina-zircon refractory.

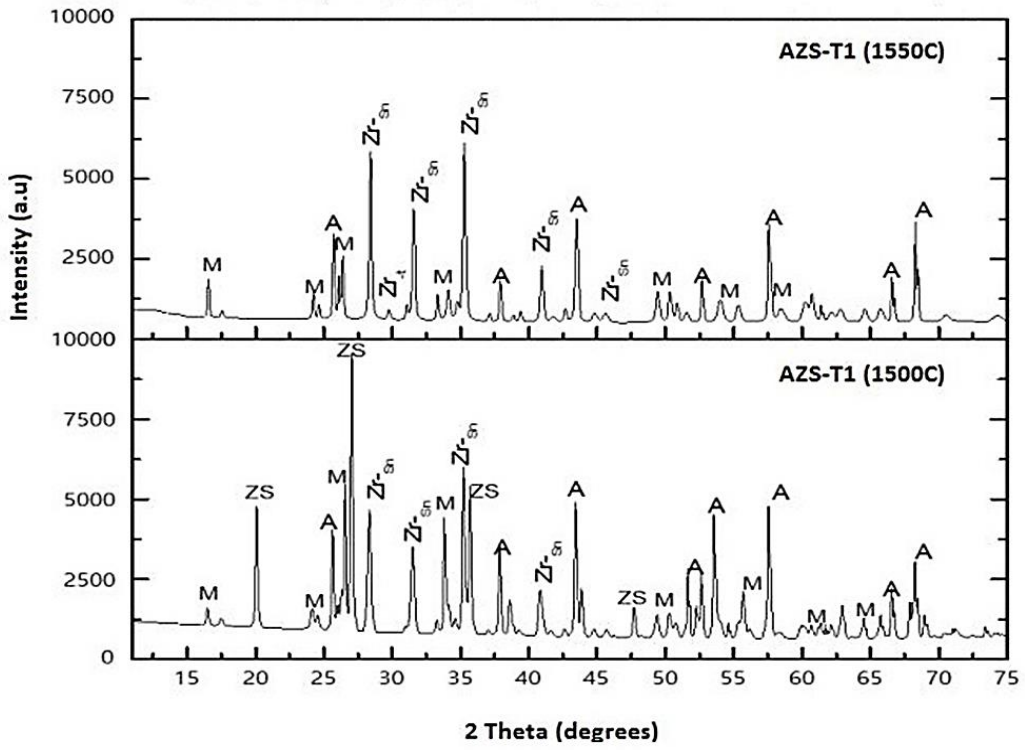

Figure 3: XRD pattern of refractory AZS-T1 and AZS-T2 sintered at 1500C and 1550C. A = a-Al_2O_3; M = $Al_6Si_2O_{13}$; Zr-Sn = $Zr_{0.93}Sn_{0.07}O_2$

Evidence of mullitisation of alumina-zircon refractory can be seen from the SEM, EDX and microstructure of the AZS-T1 refractory sample from the selected yellow highlighted square region in the SEM micrograph in figure 4 after sintering at 1500°C. The microstructure of AZS-T1 reveals a dense sintered matrix of the refractory that comprises of well dispersed composite grains of zirconia-tin oxide solid solution (bright/light grains-3), corundum grains (dark grey-2), mullite (lighter dark grey-4) and partially dissociated zircon grains (light grey grains-1). From figure 4, it can be seen that the fine-grained zircon (d_{50} = 2.5µm), has undergone a complete solid-state dissociation while the large zircon grains (d_{50} ~140µm) are partially dissociated. The solid-state dissociation products, ZrO_2 and amorphous SiO_2, reacts with SnO_2

and α-Al_2O_3 to form a $Zr_{(1-x)}Sn_xO_2$ solid solution and equiaxed mullite (MI, type 1 mullite) respectively. SEM phase quantification of the granular mullite evolved, revealed the Al_2O_3:SiO_2 ratio to be 72.06:27.94 wt. %; indicating a near stoichiometric 3:2 Mullite.

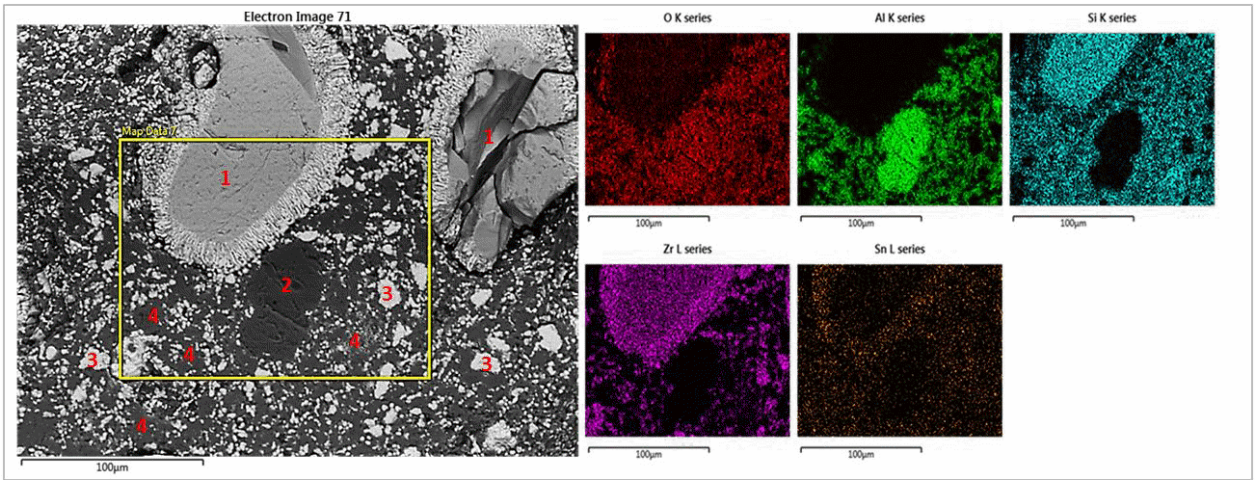

Figure 4: SEM EDX elemental mapping of AZS-T1 refractory microstructure after sintering at 1500C for 1h.
(1) Zircon (light grey grains); (2) α-Al_20_3 (Corundum dark grey grains); (3) $Zr_{1-x}Sn_xO_2$ solid solution (bright light grains); (4) 3:2 Mullite (lighter dark grey.

This is in good agreement with observations made by other studies in literature [2-4,9,10] and expected from a solid-state reaction at such low sintering temperatures in the presence of excess Al_2O_3 in the Al_2O_3:SiO_2 ratio from the starting batch mixture (Table 1). Figure 4 further shows that the partial solid-state dissociation of the large "zircon sand" grains has occurred with decomposition initiating from the zircon grain edges and progressing towards the centre. This is also in good agreement with similar observations made by other groups on the thermal dissociation of zircon and the conventional accepted theory that solid-state reactions occur faster with decreasing particle size [40]. At these zircon grain edges, precipitated SnO_2 enriched ZrO_2 dendritic grains appear where SiO_2 is depleted due to in situ mullite formation. It is known that in the silica-rich region of the SnO_2-SiO_2 system a eutectic appears at 1505 ˚C ± 5 ˚C [31]; while in the alumina rich corner of the Al_2O_3-SiO_2-ZrO_2 system, a ternary eutectic appears at 1550 ˚C; and in the presence of impurities, these eutectics may occur at even lower

temperatures [40,41]. Therefore, this suggests that the presence of SnO_2 enhances the solid-state dissociation of zircon and dissolution of the amorphous SiO_2, and because of the limited solubility of SnO_2 in the SiO_2, a $(Zr_{1-x}Sn_x)O_2$ solid solution is precipitated out in the form of dendrites. α-Al_2O_3 then reacts with the SiO_2 to form an equiaxed type 1 or primary mullite (MI).

When the sintering temperature is raised above 1500 °C, to 1550 °C the decomposition kinetics of the large zircon grains is increased with dissociation starting from the grains' edges towards the centre. This results in an increased amorphous silica and liquid phase which accelerates the dissociation rate of zircon and mass transfer where the free zirconia phase fraction reacts with the SnO_2 to form a solid solution that has limited solubility in the siliceous phase and thereby precipitating the $(Zr_{1-x}Sn_x)O_2$ solid solution as dendritic grains. This indicates that a formation of thermodynamically more stable $(Zr_{1-x}Sn_x)O_2$ solid solution in presence of SnO_2 has a marked influence in aiding the dissociation of zircon resulting into a minimisation of free energy of the system. Considering that the starting compositions of the refractories AZS-T1 and AZS-01 were produced from an alumina-zircon-cassiterite and alumina-zircon starting mix formulations in wt. % ratio of 57:38:5 and 62:38 respectively, the quantified XRD mineralogical analysis of the AZS-T1 and AZS-01samples, sintered above 1500 °C and presented in table 2 confirm these findings.

From table 2, it can be seen that no $ZrSiO_4$ fractions are present in the AZS-T1 refractory after sintering at 1550 °C. The $Al_6Si_2O_{13}$ and ZrO_2 phase fractions have increased while the corundum fraction has decreased in comparison to the starting compositions.

Table 2: Mineralogical composition of AZS-01 and AZS-T1 refractory composites after sintering at 1550 °C.

Sample	Mineralogical Composition (wt. %)							
	α-Al_2O_3	ZrO_2 (m)	(ZrO_2 (t)	SiO_2	SnO_2	$Al_6Si_2O_{13}$ (3:2 and 2:1)	$ZrSiO_4$	Amorphous

AZS-01	44.8	11.6	0.1	-	-	20.5	12.5	10.8
AZS-T1	38.3	*26.3	*0.1	-	0.5	27.7	-	6.6

*as $Zr_{(1-x)}Sn_xO_2$ solid solution

No cassiterite (SnO_2) peaks appear in the XRD pattern for both refractories. While SnO_2 is known to decompose and volatise in air above 1500 °C according to reaction,

$$SnO_{2\,(s)} \longrightarrow SnO_{(g)} + 0.5O_{2\,(g)} \quad \text{..... (3)}$$

XRF analysis of the bulk chemical compositions of the refractories AZS-T1 sintered at 1550°C shown in table 1 reveals that there is negligible Sn loss due to volatization. This can be explained by the fact that literature on binary phase diagrams of SnO_2 and $Al_2O_3/SiO_2/ZrO_2$ systems, albeit limited, reveals no chemical reactivity in the solid state between SnO_2/Al_2O_3 and or SnO_2/SiO_2 binary systems; but only for the formation of $Zr_{1-x}Si_xO_2 - Sn_{1-x}Zr_xO_2$ solid solutions from the SnO_2-ZrO_2 binary system thereby reducing the chemical potential of SnO_2 due to its stabilisation in the solid solution. Furthermore, in the Al_2O_3-SnO_2 system [32], a eutectic is observed at 98 wt. % SnO_2 at a eutectic temperature of 1893 ± 5 K (1620 °C) and in the presence of impurities such as Fe, Ca, Na and Ti oxides in a pseudo-quaternary Al_2O_3-SiO_2-ZrO_2-SnO_2 system, this can be lowered to below 1828K (1555 °C).

Therefore, the presence of both ZrO_2 and amorphous SiO_2 from the dissociated zircon grains, plus - transient eutectic liquid phases from the Al_2O_3-SnO_2-ZrO_2 and SiO_2-SnO_2 systems , may be thought to mitigate the volatilisation of SnO_2 through the formation of ZrO_2-SnO_2 solid solution and/or reduced SnO_2 diffusivity in the amorphous SiO_2 thereby benefiting the refractory properties constructively. High magnification SEM analysis of the AZS-T1 microstructure, as shown in figure 5 lends support to our hypothesis.

EDX semi-quantitative point analysis in figure 5 reveals the dark-grey grains (spectrum 4) as alumina grains and the white amorphous phase at the alumina grain boundaries as a SnO_2 rich,

ZrO_2 and Al_2O_3 amorphous phase. Figure 5 further shows the coalescence of alumina grains of differing sizes, with the large grains absorbing the small grains. This is enhanced by the presence of a SnO_2 rich ZrO_2-Al_2O_3 transient liquid phase which produces a capillary force that brings the grains together leading to densification and coarsening of the alumina grains [42].

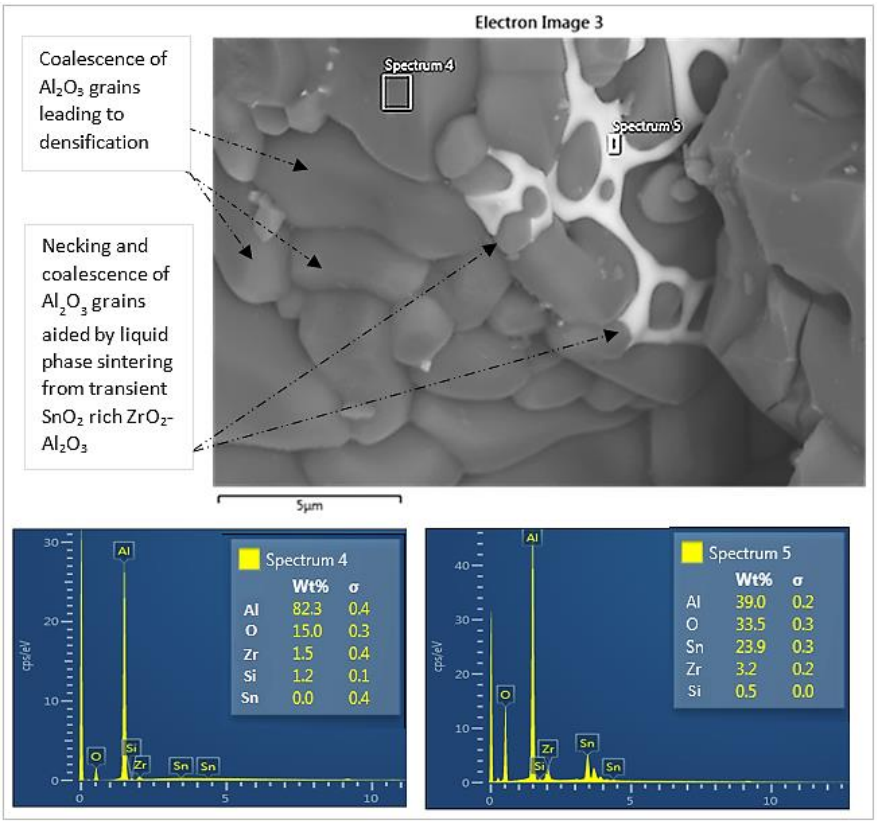

Figure 5:High magnification SEM(Hitachi SU8230) micrograph of the matrix region of the AZS-T1 refractory. A Tin oxide rich alumina-zirconia amorphous phase (white) can be seen at the grain boundaries of alumina grains (grey). Coalescence and gain growth of the alumina grains is cleary discernable and is enahanced by liquid phase sintering.

The grain coarsening and densification is aided by enhanced ionic diffusion and mass transport through the liquid phase [42]. Our findings are in good agreement with results from other workers where, for high-solid content mixtures, boundary migration was the typical mechanism and grain boundary migration was through a transient liquid layer [42, 43]. The

presence of a liquid phase in sintering is known to permeate the microstructure leading to densification [43,44].

Table 3: Bulk density (BD) and apparent porosities (AP) of AZS-01 and AZS-T1 refractories.

Sample	After sintering at 1500°C		After sintering at 1550°C	
	B.D (gcm^{-3})	**A.P** (%)	**B.D** (gcm-3)	**A.P** (%)
AZS-01	3.34	13.6	3.29	13.0
AZS-T1	3.37	12.8	3.41	8.5

Density and apparent porosity measurements of samples sintered at 1500 °C and 1550 °C shown in table 3 indicates that the bulk density of AZS-01 decreases slightly whereas the porosity remains nearly unchanged for AZS-01.However, there is a slight increase in density and significant reduction in the apparent porosities of AZS-T1.

3.3 Mullite Microstructural Evolution

Microstructure plays an important role in dictating the bulk properties of refractory materials and therefore in this study we have looked at analysing the microstructural evolution of the reaction sintered mullite in the AZS-T1 refractory. Mullite formation in reaction sintering of Al_2O_3 and SiO_2 is known to be dissolution-precipitation controlled. Hence, based on the above observations and analysis, the morphology of the evolved mullite in the microstructure of AZS-T1 refractory sintered at 1500 °C would be expected to differ from that sintered at 1550 °C. SEM microstructural analysis of the AZS-T1 refractory products sintered at 1500 °C revealed that the evolved mullite has an equiaxed granular structure. Figure 6 shows the microstructure of the AZS-T1 refractory matrix region after sintering at 1550 °C. From figure 6, it can be seen that three types of mullite, based upon their morphology and aspect ratios as defined by Iqbal and Lee [11,13] have evolved.

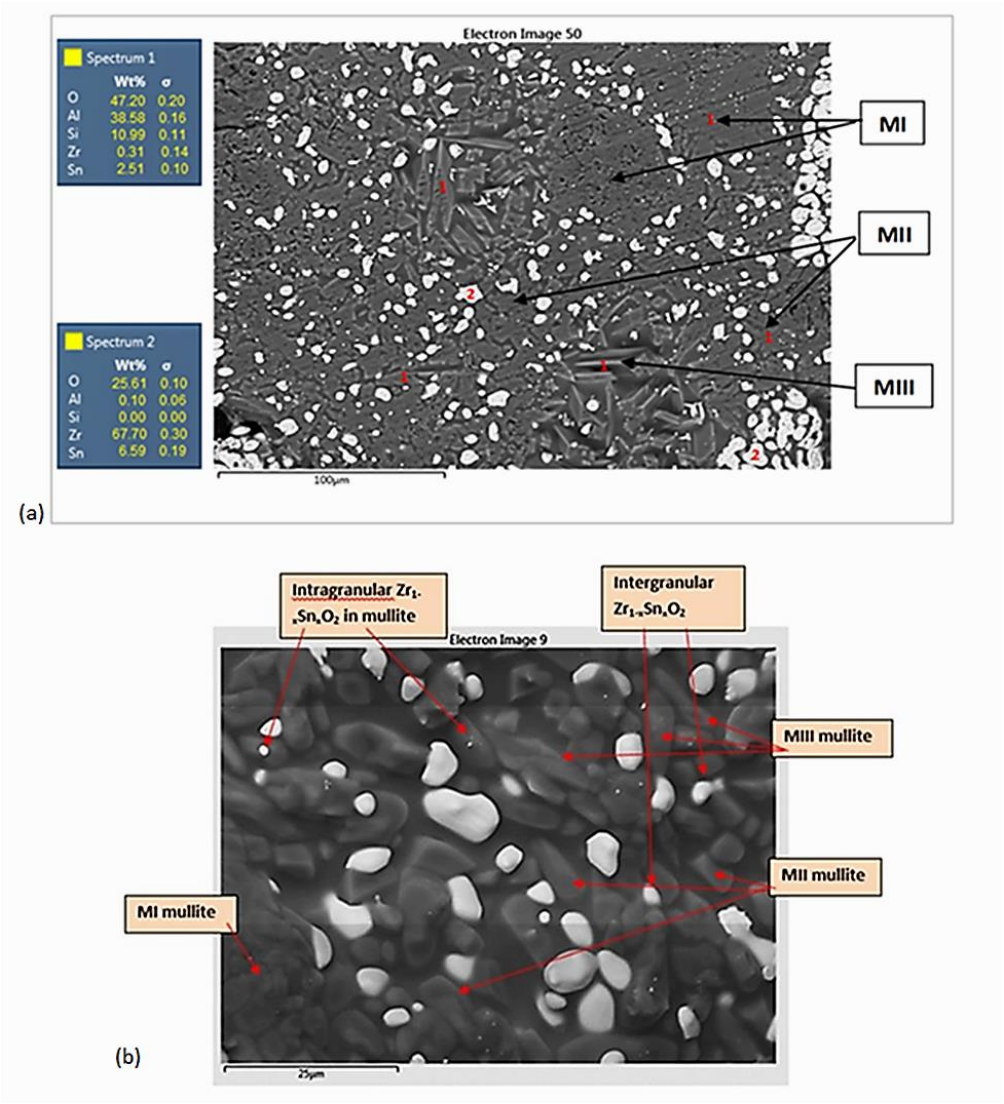

Figure 6: (a) SEM micrograph showing the microstructure of the AZS-T1 refractory; and (b) The three types of evolved mullite; MI = type 1 (primary mullite); MII = type 2 (secondary mullite); MIII = type 3 (tertiary mullite).

The proportion of the equiaxed primary mullite MI is reduced as grain growth of the primary mullite grains (MI) occurs, increasing in size with their aspect ratio reaching the maximum 3:1. It is expected and known that an increased presence of a less viscous amorphous phase with increasing temperature; and in the case of this study – an amorphous SiO_2 phase; will enhances mass transport and the potential for unhindered grain growth [41-43]. Therefore, the grain coarsening was due to the rise in sintering temperature from 1500 °C to 1550 °C as well as an increase in a less viscous transient amorphous phase from the decomposing zircon grains which

favours mass transport and grain growth. The spatial arrangement of the MI and MII mullite also suggest that the primary mullite MI transforms into MII due to an increase in both the sintering temperature and amorphous SiO_2 phase from the dissociating zircon grains. Adjacent to the secondary MII mullite are the tertiary MIII mullite grains, distinguishable by their needle like morphology and very high aspect ratio grains.

From figure 6a, it can be seen that the tertiary acicular MIII mullite occurs near agglomerates of $Zr_{1-x}Sn_xO_2$ crystals, evolved from the dissociated zircon grains. EDX semi-quantitative analysis reveals the Al_2O_3:SiO_2 ratios of MIII and MII to be 77.8:22.2 wt. % and 75.5:24.5 wt. % respectively; an increase of Al_2O_3 content in the mullite structure from the MI mullite Al_2O_3:SiO_2 ratios. This means that the mullite compositions varies from a 3:2 mullite composition (71-74 wt. % Al_2O_3) from the primary MI to a 2:1 mullite composition (> 76 wt. % Al_2O_3) from the secondary MII and tertiary MIII mullite. This suggests that the occurrence and growth of MII and tertiary MIII mullite is due to a fluid matrix, in good agreement with numerous other studies [11-13]. Furthermore, it appears in this study that an alumina-rich siliceous phase resulting from corundum dissolved in the amorphous silica produced by the dissociation of zircon allows nucleation and enhanced unhindered growth of the Mullite crystals to high aspect ratios. EDX semi-quantitative analysis reveals that the MII and MIII mullite incorporates within their structure both ZrO_2 and SnO_2. This would be expected to impart better corrosion resistant properties to the mullite grains in molten glass or slags.

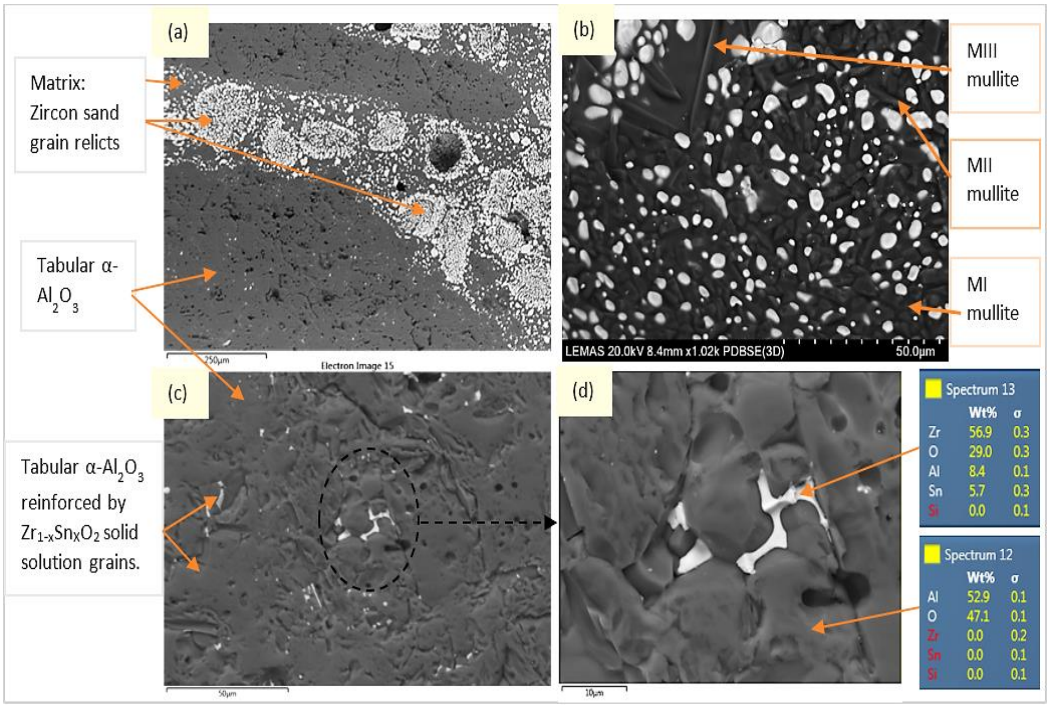

Figure 7: SEM micrographs of the AZS-T1 refractory showing its microstructure after sintering at 1550C.

(a) Micrograph shows the aggregate - tabular (α-Al_2O_3) grains in zirconia reiforced mullite matrix matrix. (b). Micrograph shows homegenous dispersion of zirconia grains within the mullite matrix. (c) Tabular α-Al_2O_3 aggreagte grain with $Zr_{(1-x)}Sn_xO_2$ dispered within the pores of the grains. (d) High mag. SEM micrograph of Tabular α-Al_2O_3 aggregate grain reinforced by $Zr_{(1-x)}Sn_xO_2$ grains.

Figure 7 (a) - (d); shows SEM micrographs of the resultant microstructures of AZS-T1 sintered at 1550 °C. From the figure 7(a), the microstructure consists of aggregate tabular alumina grains within a mullite matrix reinforced by a dispersion of zirconia agglomerates from dissociated zircon grain relics. The mullite matrix shown in figure 7 (b) reveals the homogenous dispersion of $Zr_{(1-x)}Sn_xO_2$ within the M1, MII and MIII crystals. Figure 7, (c) and (d); further reveal that the tabular alumina aggregate grains are reinforced by precipitated $Zr_{(1-x)}Sn_xO_2$ solid solution grains, possibly from the transient liquid phase filling the tabular alumina pores. Therefore, the microstructures of the AZS-T1 refractory evolve to a monoclinic $Zr_{(1-x)}Sn_xO_2$ reinforced mullite and alumina composite with some tetragonal untransformed $Zr_{(1-x)}Sn_xO_2$ remaining as a minor phase when sintered at 1550 °C.

3.4 Effect on Thermo-Mechanical Properties

The refractoriness and HMOR of the developed compositions AZS-01 and AZS-T1 were evaluated and compared to understand the effect of SnO_2 on the hot flexural strength of the AZS-T1 refractory. Table 4 shows the refractoriness or fusibility temperature range and the Pyrometric Cone Equivalent (PCE), values of the developed AZS-01 and AZS-T1 refractories.

Table 4: Refractoriness (fusibility temperature range) and PCE values of developed refractories.

Refractory - Sample	Refractoriness (°C)	PCE
AZS-01	1775 °C	34 – 35
AZS-T1	1724 – 1743 °C	32.5 – 33

AZS-01 and AZS-T1 have high refractoriness, typical of high alumina refractories [2,3,5,7,10,44]. From the chemical composition of the refractories, AZS-01 and AZS-T1 given in table 1, both refractories contain similar low concentration of flux impurities such as alkali and alkaline earth metal oxides (R_2O and RO), as well as TiO_2 and Fe_2O_3. These impurity compounds are known to introduce low melting liquid phases which affect the thermal stability of the refractory. While it is known that the fusion point of cassiterite is low (1625 ± 5 °C), when considering the refractoriness of the tin oxide incorporated refractory, AZS-T1 (1743 °C max) and that of AZS-01 without any dopant (1775 °C), it can be concluded that the addition of SnO_2 (m.p. 1625 ± 5 °C) lowers the refractoriness of the AZS refractories only by about 1.7%. This can be related to the observed microstructure, as shown in figure 6, of the evolved ZrO_2-SnO_2 solid solution and high alumina 2:1 acicular mullite grains (MII and MIII mullite), which yields a three dimensional reinforced network of the microstructure that enhances the thermal stability and resistance to shearing or deformation at high temperatures [13,44]. Under service however, refractories are constantly subjected to loads and as explained earlier, their refractoriness is lowered. Therefore, the refractoriness under load (RUL) of AZS-01, and AZS-

T1 were evaluated. Figure 8, shows the RUL curves of the developed refractory compositions AZS-01 and AZS-T1 from room temperature to 1700 °C (1973K).

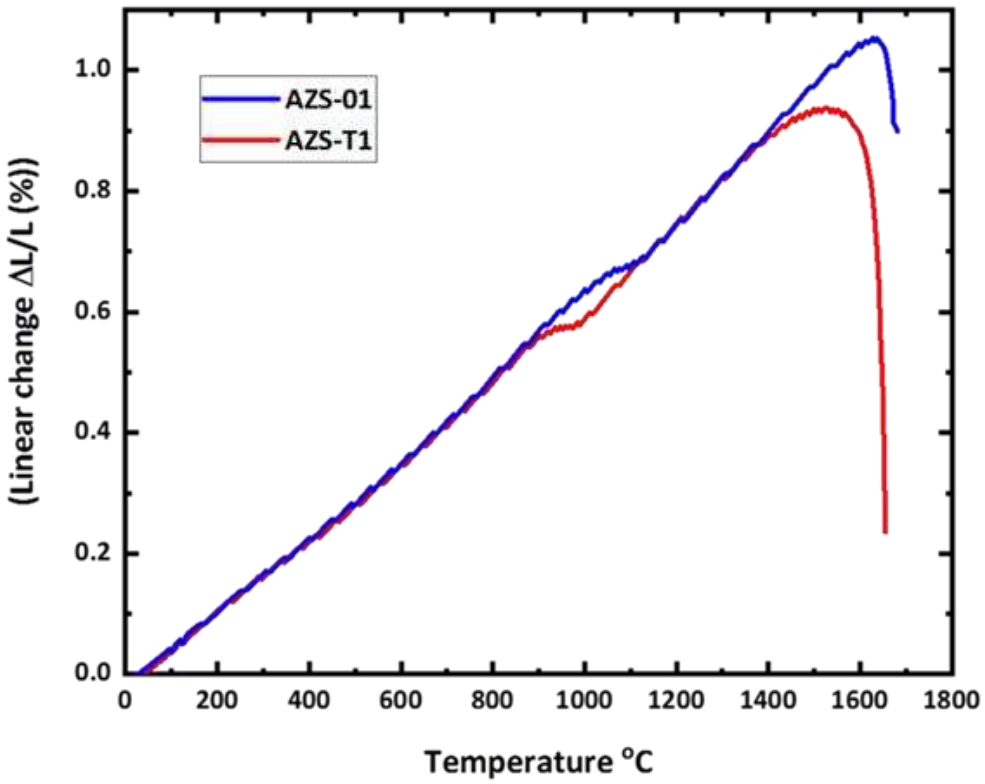

Figure 8 Refractoriness under load curves of AZS-01, AZS-T1 and AZS-T2 refractories.

There are two significant event specific temperature domains observed in figure 8, namely;

1) The linear expansion curves of AZS-01 and AZS-T1 and points of inflection that correspond to the allotropic phase transformation in zirconia; and,
2) The region of subsidence of the AZS-01 and AZS-T1 from 1350 °C – 1700 °C that presents the maximum expansion and, beginning and end of the softening temperature range.

The allotropic phase transformation of zirconia from monoclinic to tetragonal phase is known to occur in the temperature range of 950 °C to 1180 °C which is close to that observed in figure 8.

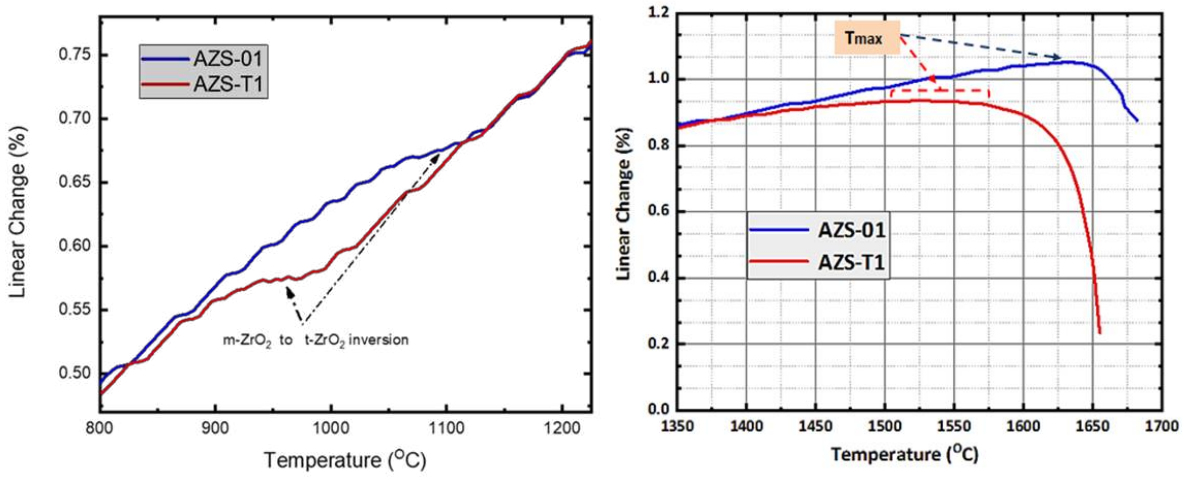

Figure 9: (a) Linear expansion curve of AZS-01 and AZS-T1 refractories showing the expansion paths of the two AZS refractories and the points of inflection that correspond to the zirconia allotropic phase transformation.
(b) Refractoriness under load curves of AZS-01, AZS-T1 refractories in the temperature range of maximum expansion and end of subsidence.

From figure 9a it can be seen that for the AZS-T1 refractory, with SnO_2 dopant, the transformation occurs between 910 °C – 980 °C; whereas for AZS-01 (without any SnO_2 additions) the phase transformation occurs between 1080 °C – 1180 °C. This decreased monoclinic – tetragonal transformation can be attributed to the formation of solid solution of SnO_2 in t-ZrO_2 which transforms to monoclinic $(Zr_{1-x}Sn_x)O_2$ as observed in the XRD pattern of AZS-T1 presented in figure 4. This occurrence is analogous to observed decreased zirconia allotropic transformations temperature from TiO_2 additions [18]. This shows that SnO_2 has a marked effect in stabilising the tetragonal phase to a much lower transformation temperature range of 910 °C – 980 °C from 1050°C - 1120°C which is beneficial for the extended high temperature durability of AZS refractories in service.

However, when considering the region of subsidence of the refractories on the RUL curve, shown in figure 9b, the effect of SnO_2 on the thermal stability of SnO_2 incorporated AZS composition (AZS-T1) can be seen from the slope of RUL-curve for AZS-T1 and the calculated RUL results presented in table 5. From table 5, the maximum expansion of AZS-T1 is reached at 1560 °C under a 0.2N Load and is maintained until 1645 °C, where subsidence of the

refractory starts. The Ta or $T_{0.5;}$ which is quoted and taken as the temperature of appearance at which 0.5% subsidence of the refractory occurs; is given as the RUL value of a refractory as this represents changes in the phases of the refractory microstructure, normally as a result of formation of low melting liquid phases.

Table 5: Calculated RUL values of the developed refractory compositions. (D_{max} = maximum expansion temperature; $T_{0.5}$ (Ta) = temperature of appearance)

Refractory	D_{max} (°C)	Linear Expansion-D_{max} (%)	$T_{0.5}$ (°C)	$T_{1.0}$ (°C)
AZS-01	1640 – 1672	1.1	>1681	>1681
AZS-T1	1560 – 1645	0.9	1651	1659

In contrast, AZS-01 reaches maximum expansion at 1640 °C and up to 1672 °C where the curve starts to taper signalling the beginning of subsidence of the refractory. This means that the AZS-01 refractory, without any SnO_2 doping, has a narrower temperature range in which it resists against high temperature stresses before subsiding, while for the AZS-T1 refractory, it presents a wider range temperature of thermal stability. This can be attributed to the formation or evolution of the acicular 2:1 mullite; with much lower and less anisotropic coefficient of thermal expansion [8], and as well forms a reinforcing interlocked network within the refractory microstructure [8,11-13].

RUL results in table 5 further shows that AZS-01 has high refractoriness under load than the SnO_2 doped compositions. This is expected based on the refractoriness or PCE values of the refractory compositions presented in table 5. The temperature of subsidence ($T_{1.0}$ or 10% of refractory slagging) of the AZS-01 is ca.1681 °C which is ca. 100 °C lower than the refractoriness values of AZS-01 presented in table 4. In comparison, the temperature of subsidence of AZS-T1 is 1622 °C. This suggests that SnO_2 dopant affects and lowers the high temperature stability of the AZS refractories by about 3%. These results show that SnO_2 as a

sintering aid does not significantly reduce the high temperature properties of the AZS refractories.

3.5 Effect on Refractory Chemical Compatibility in Soda lime Glass

The effect of the dopant, SnO_2, on the corrosion resistance of AZS refractories compositions was evaluated in SLS glass melt at 1370 °C for 72 hrs. Although, static isothermal test conditions are not experienced in actual service by the refractory materials during glass production, they were used in this initial study, simply to compare the relative corrosion resistance of the AZS-01 and AZS-T1 refractories.

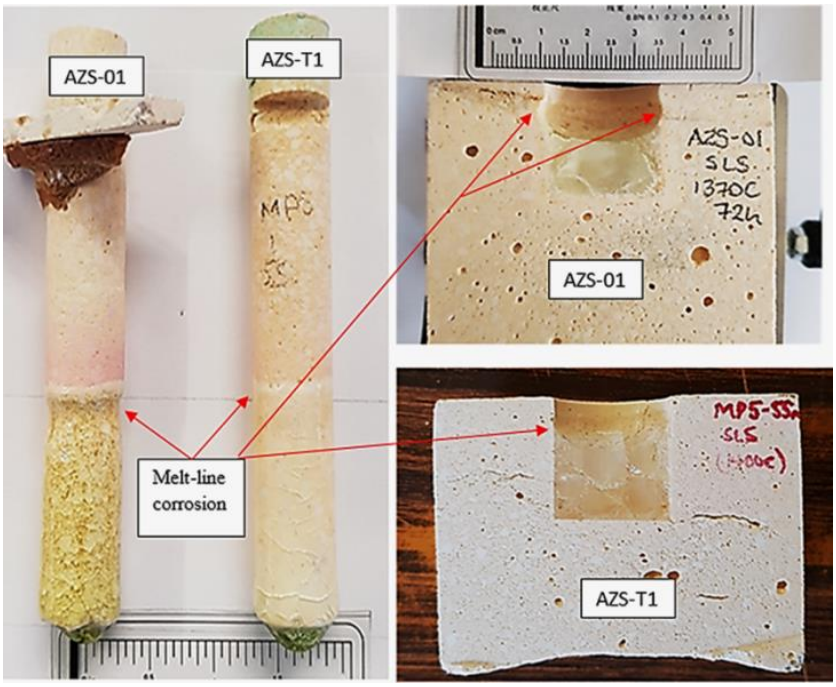

Figure 10: Static cup test samples and finger refractory samples of AZS-01 and AZS-T1 after static corrosion glass test in SLS glass. The increased corrosion resistance of the AZS-T1 refractory, doped with SnO2 compared to the AZS-01 is shown by presenting the flux/melt line corrosion cuts on the respective refractories.

Figure 10 shows the static cup test samples and finger samples of AZS-01 and AZS-T1 after static glass corrosion in SLS glass at 1370 °C for 72hr. AZS-01 presents enhanced flux line corrosion from both the sectioned static test cup samples and the finger sample, as compared to AZS-T1. This comparison shows clearly the increased corrosion resistance of SnO_2

incorporated AZS refractories. The effect of SnO_2 on the corrosion resistance of the AZS composition doped with tin dioxide was also evaluated and validated by investigating the $Zr_{1-x}Sn_xO_2$ solid solution grain from the AZS-T1 composition and the ZrO_2 grain from the AZS-01 composition that have come to chemical equilibrium with the glass after the static glass corrosion tests. Figure 11 shows the AZS-01SLS glass interface and AZS-T1-SLS glass interface respectively. Table 6 shows the SEM point EDX semi-quantitative analysis of the zirconia grains at equilibrium with the glass.

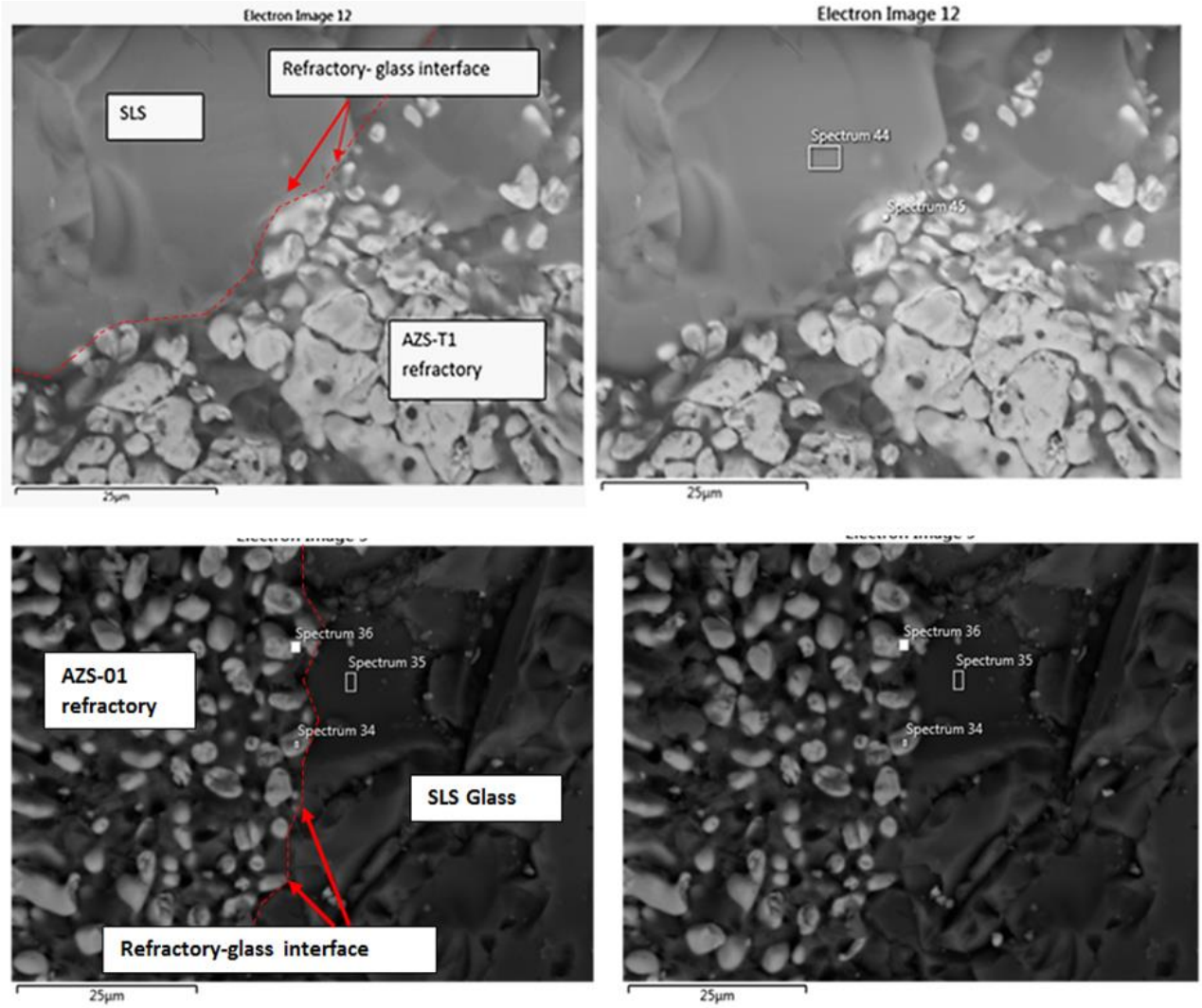

Figure 11: (a, top left-right) Refractory – Glass Interface of AZS-T1 and SLS glass; showing grains of $Zr_{1-x}Sn_xO_2$ solid solution in chemical equilibrium with the SLS glass. (b, bottom left-right) AZS-01 Refractory and SLSL Glass Interface revealing ZrO_2 grain from the AZS-01 refractory in chemical equilibrium with the SLS glass

In table 6, it is observed that about 1.1 wt. % of Zr (1.5 wt. % ZrO_2) from the $(Zr_{1-x}Sn_x)O_2$ solid solution has dissolved from the AZS-T1 refractory into the glass at the interface that makes up the boundary layer. However, no signatures of SnO_2 or Sn^{4+} ions were detected by SEM EDX quantification method to be present in the glass or at the interface. In contrast, from table 6 it is apparent that about 4.9 wt. % Zr (6.6 wt. % ZrO_2) has dissolved from the zirconia grain within the AZS-01 refractory into SLS glass at the interface. This clearly demonstrates the potential of SnO_2 stabilising ZrO_2 due to the mutual solid solution formation in AZS-T1 refractory composition. The stabilisation effect of SnO_2 also manifested in the form of reduced flux line corrosion of AZS-T1 compared with the AZS-01 in the finger and static cup tests as shown in figure 10.

Table 6: SEM EDX semi-quantitative analysis Zirconia grain in equilibrium with SLS glass highlighted in figure 11.

Element	AZS-T1	Interface	AZS-01	interface
	Grain	Glass	Grain	Glass
	Spectrum 44	Spectrum 43	Spectrum 34	Spectrum 35
	wt.%	wt.%	wt.%	wt.%
O	26.2	46.9	26.7	46.9
Al	0.00	13.2	0.0	5.8
Si	0.9	26.7	1.2	31.9
Zr	66.3	1.1	72.2	4.9
Sn	5.6	0.0	-	-
Ca	0.0	2.8	0.0	5.6
Na	0.9	9.3	0.0	4.9
Total	100.0	100.0	100.1	99.9

4 Conclusion

In this study, we have convincingly demonstrated and proved successfully the use of SnO_2 as sintering additive to develop and evolve reinforced alumina and mullite refractory composite AZS-T1 of the Alumina-Zirconia-Mullite system from reaction sintering of Alumina and

zircon starting mixtures can enhance the corrosion resistance of AZS class of refractories in contact with soda-lime-silica (SLS) glass at 1370 °C. Three types of mullite crystals classified based on the morphology and aspect ratios namely primary mullite (MI), secondary mullite (MII) and acicular tertiary mullite MIII are evolved and make up the matrix microstructure during the sintering of refractory compositions at 1550 °C. The MII and MIII mullite crystals, of 2:1 mullite composition, evolve in regions of aluminosilicate amorphous phases from the decomposed zircon grains and widely contribute to HMOR values of the refractories. The presence of a liquid phase enhances densification and mullitisation of the refractories and SnO_2 has a considerable influence in the enhancement of the kinetics of dissociation of zircon and subsequent reaction sintering of alumina and zircon refractories.

5 Acknowledgements

PMT and GMK would like to thank Parkinson Spencer Refractories Ltd, Halifax (PSR) for supplying their commercial raw materials for this study.

Declarations of interest: None.

6 References

[1]. Lee W.E. and R.E. Moore, Evolution of in Situ Refractories in the 20th Century. Journal of the American Ceramic Society. 81 (1998) 1385-1410. https://doi.org/10.1111/j.1151-2916.1998.tb02497.x

[2]. Da Luz A.P., M.A.L Braulio., V.C Pandalfelli, Refractory Castable Engineering. F.I.R.E Compendium Series. Goller Verlag. Baden-Baden, 2015.

[3]. C. Aksel, Mechanical properties and thermal shock behaviour of alumina–mullite–zirconia and alumina–mullite refractory materials by slip casting Ceram. Int. 29 (2003) 311-316. https://doi.org/10.1016/S0272-8842(02)00139-6

[4]. Aksel C., F.L. Riley, F. Konieczny, The corrosion resistance of alumina–mullite–zircon refractories in molten glass, Key Eng. Mater. 264-268 (2004) 1803-1806.

[5]. Yuan Q., J. Tan., Z. Jin, Preparation and Properties of Zirconia-Toughened Mullite Ceramics, Journal of the American Ceramic Society. 69 (1986) 265-267. https://doi.org/10.1111/j.1151-2916.1986.tb07422.x

[6]. Valle M., S. Gandolfi., M. Dondi., B. Fabbri, Effectiveness of various zirconium compounds in the body to improve the alkaline attack resistance of ceramic rollers, In Fourth Euro-Ceramics. 13 (1995) 131–136.

[7]. Sadik C., Iz-Eddine El Amrani., A. Albizane, Recent advances in silica-alumina refractory: A review, Journal of Asian Ceramic Societies. 2 (2014) 83-96,

[8]. Schneider H., J. Schreuer., B. Hildmann, Structure and properties of mullite—A review, Journal of the European Ceramic Society. 28 (2008) 329-344. https://doi.org/10.1016/j.jeurceramsoc.2007.03.017

[9]. Ebadzadeh T., Reaction sintering of multicomponent mixtures for producing ceramics containing zirconia, J. Eur. Ceram. Soc. 20 (2000) 725-729. https://doi.org/10.1016/S0955-2219(99)00148-X

[10]. Claussen N., J. Jahn, Mechanical Properties of Sintered, In-Situ Reacted Mullite-Zirconia Composites, Journal of the American Ceramic Society. 63 (1980) 228-229. https://doi.org/10.1111/j.1151-2916.1980.tb10700.x

[11]. Lee W.E., Y. Iqbal, Influence of Mixing on Mullite Formation in Porcelain, Journal of the European Ceramic Society. 21 (2001) 2583-2586. https://doi.org/10.1016/S0955-2219(01)00274-6

[12]. Lee W.E., G.P. Souza., C.J. McConville., T. Tarvornpanich., Y. Iqbal, Mullite formation in clays and clay-derived vitreous ceramics, Journal of the European Ceramic Society. 28 (2008) 465-471. https://doi.org/10.1016/j.jeurceramsoc.2007.03.009.

[13]. Iqbal, Y., W.E Lee, Microstructural Evolution in Triaxial Porcelain, Journal of the American Ceramic Society. 83 (2000) 3121-3127. https://doi.org/10.1111/j.1151-2916.2000.tb01692.x

[14]. Kumar P., M. Nath., A Ghosh., H.S Tripathi, Thermo-mechanical properties of mullite—zirconia composites: Effect of CaO, Transactions of Nonferrous Metals Society of China. 26 (2016) 2397-2403. https://doi.org/10.1016/S1003-6326(16)64329-7

[15]. Tripathi H.S., G. Banerjee, Synthesis and Mechanical Properties of Mullite from beach sand sillimanite: Effect of TiO_2, Journal of the European Ceramic Society. 18 (1998) 2081-2087. https://doi.org/10.1016/S0955-2219(98)00149-6.

[16]. Sarkar R., M Mallick, Formation and densification of mullite through solid-oxide reaction technique using commercial-grade raw materials, Bull Mater Sci. 41 (2018). https://doi.org/10.1007/s12034-017-1533-7

[17]. Melo M.F., M.O Figueiredo, Behaviour of titanium in mullite– zirconia composites, Materials Science and Engineering A. 109 (1989) 61-68. https://doi.org/10.1016/0921-5093(89)90565-0.

[18]. Ebadzadeh T., E. Ghasemi, Effect of TiO_2 addition on the stability of t-ZrO_2 in mullite–ZrO_2 composites prepared from various starting materials, Journal of Ceramics International. 28 (2002) 447-450. https://doi.org/10.1016/S0272-8842(01)00117-1.

[19]. Maitra S., S. Pal., S. Nath., A. Panday., R Lodha, Role of MgO and Cr_2O_3 additives on the properties of zirconia–mullite composites, Journal of Ceramics International. 28 (2002) 819-826. https://doi.org/10.1016/S0272-8842(02)00048-2.

[20]. Pena P., J.S Moya., S De Aza., E. Cardinal., F. Cambier., C. Leblud, M.R Anseau, Effect of magnesia addition on the reaction sintering of zirconia/alumina mixtures to produce zirconia toughened mullite, Journal of Materials Science Letters. 2 (1983) 772-774. https://doi.org/10.1007/BF00720556.

[21]. Kumar P., M. Nath., A. Ghosh., H.S Tripathi, Enhancement of thermal shock resistance of reaction sintered mullite–zirconia composites in the presence of lanthanum oxide, Materials Characterization. 101 (2015) 34-39. https://doi.org/10.1016/j.matchar.2015.01.004.

[22]. Das K., G. Banergee, Mechanical properties and microstructures of reaction sintered mullite–zirconia composites in the presence of an additive — dysprosia, Journal of the European Ceramic Society. 20 (2000) 153-171. https://doi.org/10.1016/S0955-2219(99)00147-8

[23]. Hong S.H., W. Cermignani., G.L. Messing, Anisotropic grain growth in seeded and B_2O_3-doped diphasic mullite gels, Journal of the European Ceramic Society. 16 (1996) 133-141. https://doi.org/10.1016/0955-2219(95)00144-1

[24]. Kong, L.B., Y.B Gan., J Ma., T.S Zhang., F Boey., R.F Zhang, Mullite phase formation and reaction sequences with the presence of pentoxides, Journal of Alloys and Compounds - J Alloys Compounds. 351 (2003) 264-272. https://doi.org/10.1016/S0925-8388(02)01044-7.

[25]. Gaillard-Allemand B., R. Podor., M. Vilasi., C. Rapin., A. Maıtre., P. Steinmet, Experimental study of the SnO_2-ZrO_2 phase diagram, Journal of the European Ceramic Society. 22 (2002) 2797–2803. https://doi.org/10.1016/S0955-2219(02)00034-1

[26]. Ma J., Y. Zhu., J Wei, X. Cai., Y. Xie, Lean NOx reduction over $Sn_{1-x}Zr_xO_2$ solid solutions, Studies in Surface Science and Catalysis, Elsevier. 130 (2000) 617-622. https://doi.org/10.1016/S0167-2991(00)81026-5

[27]. Kim D.J., J.W. Jang., H.L Lee, Effect of Tetravalent Dopants on Raman Spectra of Tetragonal Zirconia, Journal of the American Ceramic Society. 80 (1997) 1453-1461. https://doi.org/10.1111/j.1151-2916.1997.tb03003.x

[28]. Hunter B.A., C.J. Howard., D.J. Kim, Bond Valence Analysis of Tetragonal Zirconia's, Journal of Solid-State Chemistry. 146 (1999) 363-368. https://doi.org/10.1006/jssc.1999.8363.

[29]. Jagadish C.R., C.R. Saha., P. Pramanik, Chemical synthesis of nanocrystalline tin doped cubic ZrO_2 powders, Materials Letters. 57 (2003) 2140-2144. https://doi.org/10.1016/S0167-577X(02)00708-5.

[30]. Kong L.B., T.S. Zhang., J. Ma., F. Boey, Some main group oxides on mullite phase formation and microstructure evolution, Journal of Alloys and Compounds. 359 (2003) 292-299. https://doi.org/10.1016/S0925-8388(03)00193-2

[31]. Yin T., Coupled Thermodynamic Modelling and Experimental Study of SnO_2-SnO-CaO-SiO_2 system: Thesis. Department of Mining and Materials Engineering McGill University, Montreal, Canada, 2017.

[32]. Barczak V. J., R.H. Insley, Phase Equilibria in the System Al_2O_3,-SnO_2,. J. Am. Ceram. Soc. 45 (1962) 144-144

[33]. Manfredo, L. J., R.N. McNally., Solubility of Refractory Oxides in Soda Lime Glass, Journal of the American Ceramic Society. 67 (1984) 155-158. https://doi.org/10.1111/j.1151-2916.1984.tb19178.x

[34]. Toperesu M.P., W Kusepile, G Kale, J Daji and D Parkinson. Hot Corrosion Behaviour of Sintered AZS Refractories in Special (Type 1, Class A) Glass Melt with Increasing Soda Content. (2020), Unpublished preliminary research.

[35]. Sarkar R. Particle Size Distribution for Refractory Castables: A Review, Interceram. - Int. Ceram. Rev. 65, (2016) 82–86. https://doi.org/10.1007/BF03401156

[36]. ASTM C830-00, Standard Test Methods for Apparent Porosity, Liquid Absorption, Apparent Specific Gravity, and Bulk Density of Refractory Shapes by Vacuum Pressure. (2016).

[37]. ASTM C133-97, Standard Test Methods for Cold Crushing Strength and Modulus of Rupture of Refractories, ASTM International, West Conshohocken, PA, (2015), (2015). www.astm.org

[38]. ASTM C24-09, Standard Test Method for Pyrometric Cone Equivalent (PCE) of Fireclay and High-Alumina Refractory Materials, ASTM International, West Conshohocken, PA, (2018). www.astm.org

[39]. Sudarminto H.S., K. Sakamoto, Y. Tsuchiuchi., M. Sugisaki, Segregation of Tin Oxide in Oxide Layer of Zircaloy-type Alloys, Journal of Nuclear Science and Technology. 39 (2002) 150-155. https://doi.org/10.1080/18811248.2002.9715168

[40]. Pavlik R.S., H.J. Holland., E.A. Payzant. Thermal Decomposition of Zircon Refractories, Journal of the American Ceramic Society. 84 (2001) 2930-2936. https://doi.org/10.1111/j.1151-2916.2001.tb01117.x

[41]. Kaiser A, M. Lobert., R. Telle, Thermal Stability of Zircon ($ZrSiO_4$), Journal of the European Ceramic Society. 28 (2008) 2199-2211. https://doi.org/10.1016/j.jeurceramsoc.2007.12.040.

[42]. German R.M, P. Suri., S.J. Park, Review: Liquid Phase Sintering, Journal of Materials Science. 44 (2008) 1-39. https://doi.org/10.1007/s10853-008-3008-0

[43]. Kozma L, W. Huppmann., L. Bartha., P. Mezei, Initiation of Directional Grain Growth during Liquid-Phase Sintering of Tungsten and Nickel, Journal of Powder Metallurgy. 24 (1981) 7-11. https://doi.org/10.1179/pom.1981.24.1.7

[44]. Courtney T.H., Densification and structural development in liquid phase sintering, Journal of Metallurgical and Materials Transactions A. 15 (1984) 1065–1074. https://doi.org/10.1007/BF02644699

[45]. Khandelwal S.K., R.L. Cook, Effect of alumina additions on crystalline constituents and fired properties of electrical porcelain, Am. Ceram. Soc. Bull. 49 (1970) 522-526.

1 List of Figures

the pores of the grains. (d) High mag. SEM micrograph of Tabular α-Al_2O_3 aggregate grain reinforced by $Zr_{(1-x)}Sn_xO_2$ grains.

8. **Figure 8:** Refractoriness under load curves of AZS-01, AZS-T1 and AZS-T2 refractories.

9. **Figure 9:** (a) Linear expansion curve of AZS-01 and AZS-T1 refractories showing the expansion paths of the two AZS refractories and the points of inflection that correspond to the zirconia allotropic phase transformation.

   (b) Refractoriness under load curves of AZS-01, AZS-T1 refractories in the temperature range of maximum expansion and end of subsidence.

10. **Figure 10:** Static cup test samples and finger refractory samples of AZS-01 and AZS-T1 after static corrosion glass test in SLS glass.
11. **Figure 11:** (a) Refractory – Glass Interface of AZS-T1 and SLS glass; showing grains of Zr1-xSnxO2 solid solution in chemical equilibrium with the SLS glass. (b) AZS-01 Refractory and SLSL Glass Interface revealing ZrO2 grain from the AZS-01 refractory in chemical equilibrium with the SLS glass

2 List of Tables

1) Table 1: Chemical composition of AZS-01 and AZS-T1 refractories sintered at 1550°C by XRF.

Sample	Chemical Composition (wt. %)								
	Al_2O_3	SiO_2	ZrO_2	SnO_2	*R_2O	**RO	Fe_2O_3	TiO_2	Others
AZS-01	61.8	12.8	24.9	-	0.21	0.08	0.06	0.09	<0.12
AZS-T1	57.79	12.96	24.55	4.02	0.2	0.08	0.06	0.1	<0.32

* $R_2O = Na_2O + K_2O$; ** RO = CaO

2) Table 2: Mineralogical composition of AZS-01 and AZS-T1 refractory composites after sintering at 1550 °C.

Sample	**Mineralogical Composition (wt. %)**							
	α-Al_2O_3	ZrO_2 (m)	(ZrO_2 (t)	SiO_2	SnO_2	$Al_6Si_2O_{13}$ (3:2 and 2:1)	$ZrSiO_4$	Amorphous
AZS-01	44.8	11.6	0.1	-	-	20.5	12.5	10.8
AZS-T1	38.3	*26.3	*0.1	-	0.5	27.7	-	6.6

*as $Zr_{(1-x)}Sn_xO_2$ solid solution

3) Table 3: Bulk density (BD) and apparent porosities (AP) of AZS-01 and AZS-T1 refractories.

Sample	After sintering at 1500°C	After sintering at 1550°C

	B.D (gcm^{-3})	**A.P** (%)	**B.D** (gcm-3)	**A.P** (%)
AZS-01	3.34	13.6	3.29	13.0
AZS-T1	3.37	12.8	3.41	8.5

4) ***Table 4: Refractoriness (fusibility temperature range) and PCE values of developed refractories.***

Refractory - Sample	**Refractoriness (°C)**	**PCE**
AZS-01	1775 °**C**	34 – 35
AZS-T1	1724 – 1743 °**C**	32.5 – 33

5) ***Table 5: Calculated RUL values of the developed refractory compositions.*** ***(D_{max} = maximum expansion temperature; $T_{0.5}$ (Ta) = temperature of appearance).***

Refractory	**D_{max}** (°C)	**Linear Expansion-D_{max}** (%)	**$T_{0.5}$** (°C)	**$T_{1.0}$** (°C)
AZS-01	1640 – 1672	1.1	>1681	>1681
AZS-T1	1560 – 1645	0.9	1651	1659

6) ***Table 6: SEM EDX semi-quantitative analysis Zirconia grain in equilibrium with SLS glass highlighted in figure 7-8 and 7-9.***

Element	**AZS-T1**	**Interface**	**AZS-01**	**interface**
	Grain	Glass	Grain	Glass
	Spectrum 44	Spectrum 43	Spectrum 34	Spectrum 35
	wt.%	wt.%	wt.%	wt.%
O	26.2	46.9	26.7	46.9
Al	0.00	13.2	0.0	5.8
Si	0.9	26.7	1.2	31.9
Zr	66.3	1.1	72.2	4.9
Sn	5.6	0.0	-	-
Ca	0.0	2.8	0.0	5.6
Na	0.9	9.3	0.0	4.9
Total	100.0	100.0	100.1	99.9